

A deeper look into the structure of Λ CDM haloes: correlations between halo parameters from Einasto fits

Silviu M. Udrescu^{1*}, Aaron A. Dutton^{1†}, Andrea V. Macciò^{1,2‡}, Tobias Buck²

¹New York University Abu Dhabi, PO Box 129188, Saadiyat Island, Abu Dhabi, United Arab Emirates

²Max Planck Institute für Astronomie, Königstuhl 17, 69117 Heidelberg, Germany

14 November 2018

ABSTRACT

We used high resolution dark matter only cosmological simulations to investigate the structural properties of Lambda Cold Dark Matter (Λ CDM) haloes over cosmic time. The haloes in our study range in mass from $\sim 10^{10}$ to $\sim 10^{12}M_{\odot}$, and are resolved with 10^5 to 10^7 particles. We fit the spherically averaged density profiles of DM haloes with the three parameter Einasto function. For our sample of haloes, the Einasto shape parameter, α , is uncorrelated with the concentration, c , at fixed halo mass, and at all redshifts. Previous reports of an anti-correlation are traced to fitting degeneracies, which our fits are less sensitive to due to our higher spatial resolution. However, for individual haloes the evolution in α and c is anti-correlated: at redshift $z = 7$, $\alpha \simeq 0.4$ and decreases with time, while $c \simeq 3$ and increases with time. The evolution in structure is primarily due to accretion of mass at larger radii. We suggest that α traces the evolutionary state of the halo, with dynamically young haloes having high α (closer to a top-hat: $\alpha^{-1} = 0$), and dynamically relaxed haloes having low α (closer to isothermal: $\alpha = 0$). Such an evolutionary dependence reconciles the increase of α vs peak height, ν , with the dependence on the slope of the power spectrum of initial density fluctuations found by previous studies.

Key words: cosmology: theory – dark matter – galaxies: formation – galaxies: structure – methods: numerical

1 INTRODUCTION

Accurately predicting structural properties of cold dark matter (CDM) haloes is one of the fundamental goals of modern cosmology. Predictions can be used to test CDM using rotation curves (e.g. Moore 1994; de Blok et al. 2008), and as inputs to analytic and semi-analytic galaxy formation models (e.g. Dutton et al. 2007; Dutton & van den Bosch 2009). Due to the non-linear nature of the problem, the standard approach is direct computation, starting from primordial density fluctuations, and evolving the system under the influence of gravity.

Early simulations found a central cusp with density profile $\rho \propto r^{-1}$ (Dubinski & Carlberg 1991). This is similar to the Hernquist profile (Hernquist 1990) commonly used to model the stellar distribution in elliptical galaxies. Over large radii DM haloes are more extended, and are better described by a two parameter NFW profile with inner slope

-1 , and outer slope -3 (Navarro et al. 1996, 1997). A common parameterization is to use the halo mass, M , and the concentration parameter, c , which is the ratio between the virial radius and the characteristic scale radius, and is hence dimensionless. Concentration and mass are highly correlated (Bullock et al. 2001; Macciò et al. 2007), so that to first order the structure of CDM haloes depend just on the halo mass.

The dependence of halo concentration on mass, redshift, and cosmological parameters has been the subject of extensive computational study. Recent work has shown that the three parameter Einasto profile (Einasto 1965)

$$\frac{\rho_{\text{EIN}}}{\rho_{-2}} = \exp \left\{ -\frac{2}{\alpha} [(r/r_{-2})^{\alpha} - 1] \right\}, \quad (1)$$

provides a better description of CDM density profiles than either NFW (Gao et al. 2008; Dutton & Macciò 2014; Navarro et al. 2010; Klypin et al. 2016) or a three parameter generalized NFW (Klypin et al. 2016).

The extra parameter relative to an NFW profile, α , controls the deviation from an isothermal distribution (i.e., $\rho = r^{-2}$): $\alpha = 0$ corresponds to an isothermal profile, while $\alpha = 2$ corresponds to a Gaussian, and $\alpha = \infty$ corresponds

* E-mail: smu226@nyu.edu

† E-mail: dutton@nyu.edu

‡ E-mail: maccio@nyu.edu

to a uniform density sphere. Thus haloes with larger α have less mass at small and large radii relative to haloes with lower α .

The shape parameter is an increasing function of halo mass and redshift. Strikingly the dependence with redshift is completely removed when the halo mass is replaced with the dimensionless peak height of the halo (Gao et al. 2008; Prada et al. 2012; Dutton & Macciò 2014; Klypin et al. 2016). This peak height, ν , is defined by

$$\nu(M, z) = \delta_{\text{crit}}(z)/\sigma(M, z), \quad (2)$$

where $\delta_{\text{crit}}(z)$ is the linear density threshold for collapse at redshift z , and $\sigma(M, z)$ is the rms linear density fluctuation at z within spheres of mean enclosed mass, M . The parameter $\nu(M, z)$ is related to the abundance of objects of mass M at redshift z . The characteristic mass $M_*(z)$ of the halo mass distribution at redshift z is defined through $\nu(M_*, z) = 1$. Thus, haloes with $\nu = 1$ are typical haloes and have $\alpha \simeq 0.16$ at all redshifts, while haloes with $\nu = 3$ are rare 3σ high fluctuations, and have $\alpha \simeq 0.25$.

Cen (2014) outlined how the Sérsic profile (which has the same functional form as the Einasto profile, but applied to a 2D density) could naturally arise out of a Gaussian random field. Based on this, Nipoti (2015) ran cosmological simulations and found a relation between the shape of the dark matter density profile with the index of the power spectrum of initial density fluctuations. Haloes formed in a universe with flat spectra (e.g., $n = 0$) have the mass in fewer larger clumps, while haloes formed from steep spectra (e.g., $n = -3$) have a larger amount of the mass in small clumps. Flat spectra resulted in lower $\alpha \simeq 0.1$ vs $\alpha \simeq 0.3$ for steep spectra. Qualitatively similar results have been reported by Ludlow & Angulo (2017) using power-law initial power spectra (lower- n results in higher α at fixed peak height).

Based on this insight, since higher mass haloes form on scales where n is larger, one would nominally predict that high mass haloes should have slightly lower α . However, exactly the opposite is seen in cosmological simulations: higher mass haloes have significantly higher α (Gao et al. 2008; Prada et al. 2012; Dutton & Macciò 2014).

There are structural differences between haloes of different masses: more massive haloes are, on average, less concentrated by $\simeq 0.1$ dex per decade in halo mass. If less concentrated haloes have higher α this would help explain why we don't see α decrease with increasing halo mass or peak height. Indeed, (Ludlow et al. 2013) reported a negative correlation: haloes offset to high c from the concentration mass relation had lower α while haloes offset to low c had higher α . This correlation seems to be consistent with the fact that young haloes (i.e., high peak heights, ν) are known to have low c and high α (Dutton & Macciò 2014). At issue is the relatively low resolution of the simulated haloes and thus the sensitivity to a fitting degeneracy between c and α .

In this paper we investigate further the correlations between Einasto shape parameter and concentration and the evolution of these parameters with time. We use zoom-in simulations in order to obtain much higher spatial resolution than is possible with cosmological volumes. We use two sets of simulations: Milky Way mass haloes with ~ 10 million particles per halo, and dark matter only counterparts to the NIHAO suite with ~ 1 million particles per halo.

This paper is organized as follows: in Section 2 we will

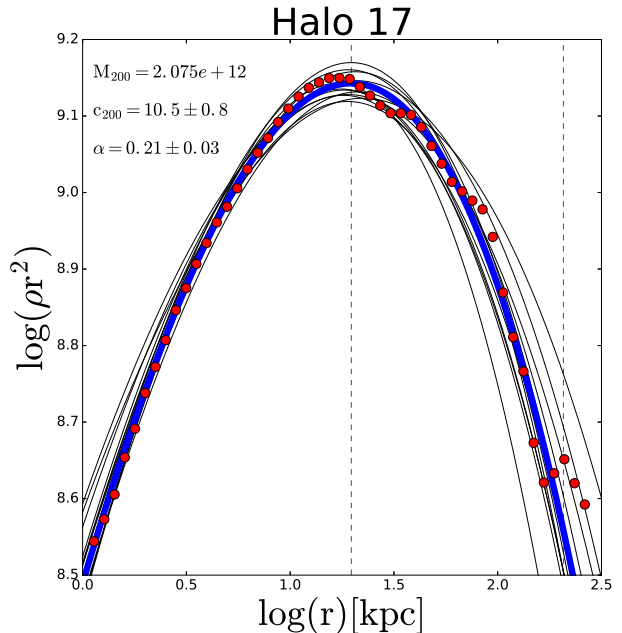


Figure 1. Example of an Einasto fit to a $10^{12} M_{\odot}$ halo (thick blue line). The red points show the density profile computed in 50 logarithmically spaced bins from three times the softening length to twice the virial radius. The green dashed line marks the position of the scale radius, r_{-2} and the virial radius, R_{200} is marked by the magenta dashed line. The grey lines represents 12 samples from the chain, obtained during the fitting procedure.

briefly summarize the properties of the simulations, in Section 3 we present the scaling relations, while in Section 4 we present the evolution of the most massive halo in each simulation. In Section 5 we discuss our results and then conclude with a summary in Section 6.

2 SIMULATIONS

We primarily use simulations from two projects. The Buck et al. (2015, 2016) study of 21 haloes of present day mass $\sim 10^{12} M_{\odot}$, and the dark matter only counterparts of the NIHAO (Wang et al. 2015) study of 91 haloes of present day masses from $\sim 10^{10}$ to $\sim 10^{12} M_{\odot}$. Each halo is simulated using the “zoom-in” technique, so there is one main halo per simulation, plus several field haloes within the zoom-in region. The main halo contains ~ 1 million particles in NIHAO, and ~ 10 million particles in Buck et al.

Haloes were identified using the MPI+OpenMP hybrid halo finder AHF¹ (Gill et al. 2004; Knollmann & Knebe 2009). AHF locates local over-densities in an adaptively smoothed density field as prospective halo centers. The virial masses of the haloes are defined as the masses within a sphere whose average density is 200 times the cosmic critical matter density, $\rho_{\text{crit}} = 3H_0^2/8\pi G$. The virial mass, size and circular velocity of the hydro simulations are denoted: $M_{200}, R_{200}, V_{200}$.

¹ <http://popia.ft.uam.es/AMIGA>

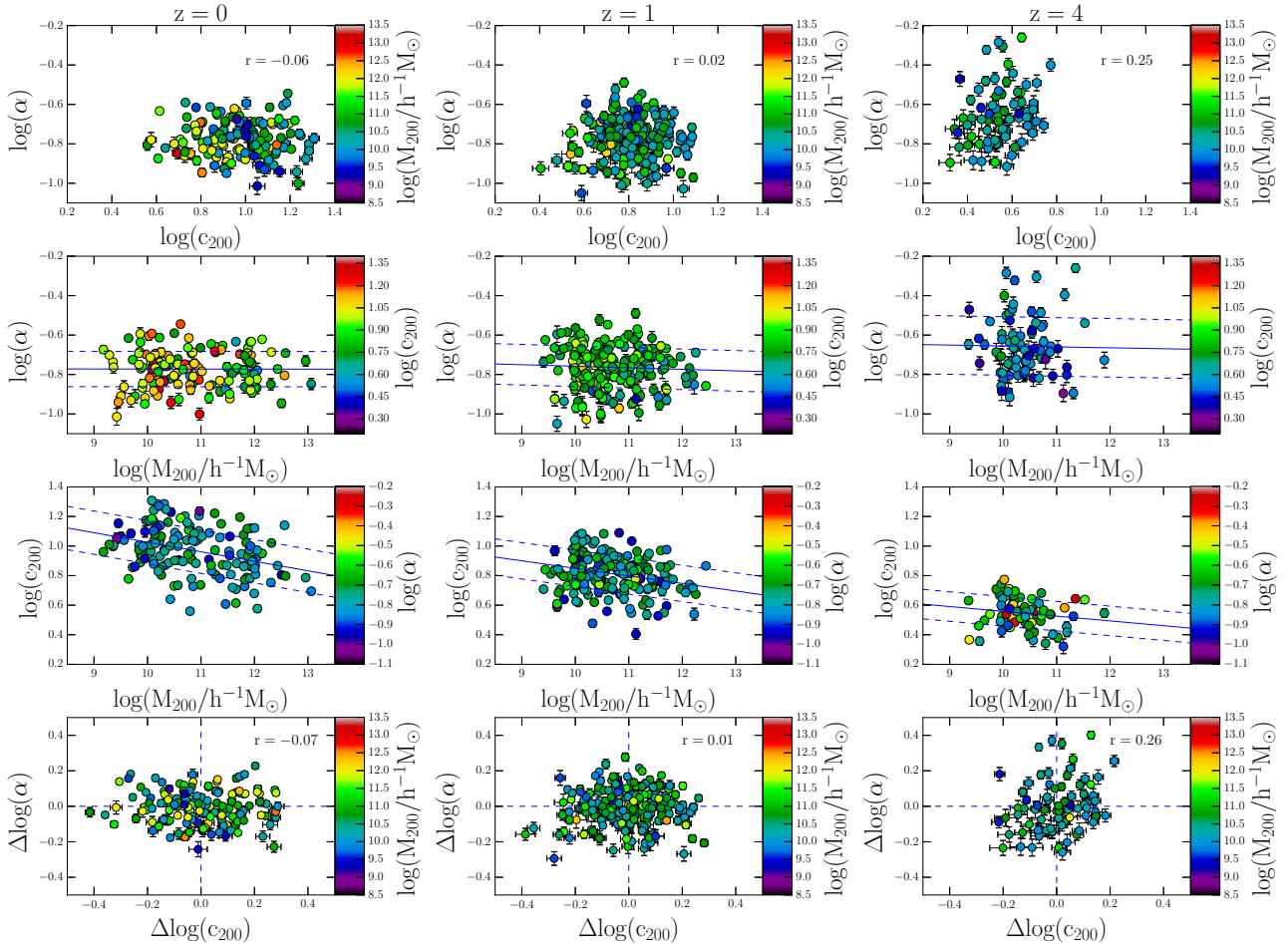


Figure 2. Relations between concentration, c , Einasto shape parameter, α and halo mass, M_{200} , at redshifts $z = 0$ (left), $z = 1$ (middle), and $z = 4$ (right). We include only relaxed, non-polluted haloes with at least 10^5 particles. Points are colour coded by the 3rd parameter (right colour-bar axis). The bottom row shows the residuals of the c vs M_{200} and α vs M_{200} relations at each redshift. These plots show there is no significant correlation between c and α .

Power et al. (2003) gave a number of convergence criteria for N-body simulations. For our purposes the strictest requirement is the relaxation time (their equation 20). For resolving the scale radius, this can be approximated with $N_{\min} = 16000(c_{200}/10)^2$ (Dutton & Macciò 2014). In order to constrain the α parameter, we wish to resolve scales significantly smaller than r_{-2} . Thus we impose a minimum particle number of $N_{\min} = 10^5$. For the Buck et al. haloes this results in a minimum halo mass of $\sim 10^{10} M_{\odot}$. We require that the mass fraction of low-resolution (i.e., polluting) particles be $f_{\text{poll}} < 10^{-3}$.

In order to filter out merging haloes (which have ill defined structural parameters) we measure two parameters related to relaxation state of the halo following (Macciò et al. 2007), x_{off} which is the distance between the most bound particle and the center of mass, in units of the virial radius, and ρ_{rms} which is the mean deviation ($\log_{10} \rho_{\text{dm}}$) between data and fit. For our relaxed halo criteria we adopt $x_{\text{off}} < 0.1$, and $\rho_{\text{rms}} < 0.1$. We also put cuts on the error in log space of c_{200} and α , such that $e_{\log c} < 0.05$ and $e_{\log \alpha} < 0.05$. In the end, out of the initially selected haloes,

we kept for analysis 74% at redshift $z = 0$, 56% at $z = 1$ and 41% at $z = 4$.

2.1 Fitting procedure

Spherically averaged density profiles were computed for all haloes that pass the described filters. For each halo, the space between 3 times the softening length and $1.5 R_{200}$ was divided into 50 shells, equally spaced in log radius. In order to obtain the density profile, for each shell the distance from the center was calculated as the average of the inner and the outer radius of the shell, while the density of the shell was computed using the mass of all the particle inside the shell and its volume.

We fit each halo with the three parameter Einasto function (Eq. 1) which is specified by the shape parameter, α , scale radius, r_{-2} , and normalization, ρ_{-2} . Since fitting the Einasto function is non-linear, we use the Monte Carlo Markov Chain (MCMC) code EMCEE (Foreman-Mackey et al. 2013) to properly sample the posterior distribution. Initial best fit parameters are obtained using the iMinuit package. The Priors for EMCEE are uni-

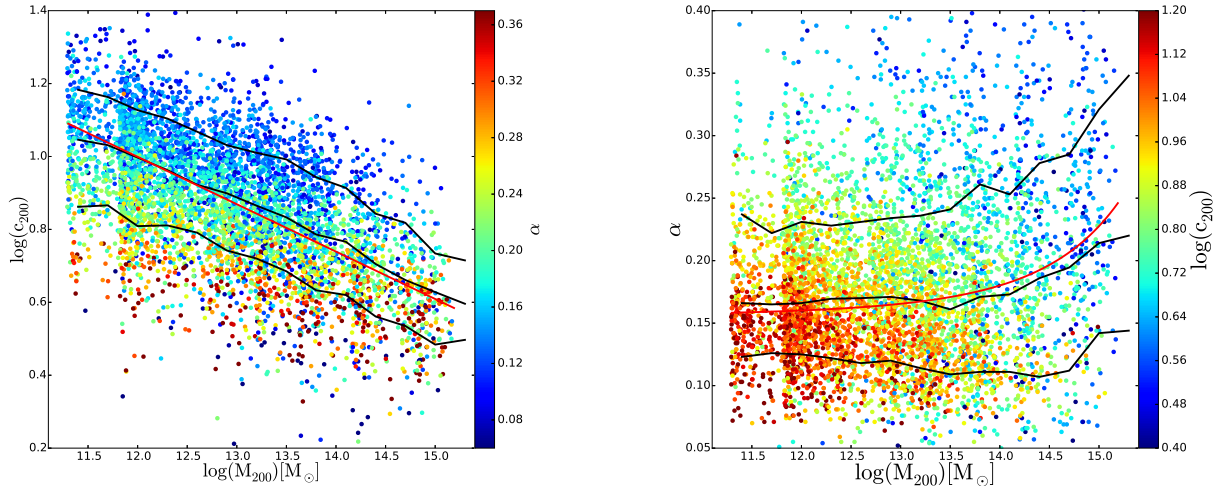


Figure 3. Concentration vs halo mass (left) and Einasto shape parameter vs halo mass (right) from low resolution ($N \sim 10000$) cosmological volume simulations (Dutton & Macciò 2014). The points are colour coded according to α (left) and c (right), showing a clear anti-correlation between α and c at fixed halo mass. The black lines show the 16th, 50th, and 84th percentiles in bins of halo mass. The red lines show the relations from Dutton & Macciò (2014) (top) and Gao et al. (2008) (bottom).

form from 0.1 to 10 times the initial best fit. The best fit value from EMCEE is taken as median of the distribution, providing better fits than the ones obtained from the iMinit results. The errors on the parameters for each fit are taken to be the 16th and the 84th percentile of the posterior distribution for the given parameter.

An example fit is shown in Fig. 1. The blue line is the obtained fit to the data, while the grey lines show 12 samples obtained from the chain, during the fitting procedure. The green and magenta dashed lines mark the scale radius, r_{-2} and virial R_{200} , respectively. Note that the concentration is computed using the virial radius from the particle data (rather than from the fitted profile), so is equivalent to the scale radius from the fit, but has an advantage of being dimensionless.

3 SCALING RELATIONS

Fig. 2 shows the relations between concentration, c , shape parameter, α , and halo mass, M_{200} , at redshifts $z = 0, 1$, and 4. The c vs mass relation and α vs mass relation have slopes, normalizations and evolutions in line with previous studies (e.g., Dutton & Macciò 2014).

We test for a correlation between α and c using two plots. The upper panels show a direct comparison, while the lower panels show the residuals of the c vs M_{200} and α vs M_{200} relations. We find no significant correlation between α and c using either method at all redshifts (the correlation coefficients are shown in the top right corner of each panel). We have verified this lack of a correlation also exists when we include unrelaxed haloes, and when we use less strict relaxation criteria. Our result should be compared with Fig. 2 in (Ludlow et al. 2013), which shows a strong anti-correlation between α and c .

In order to reproduce the result from Ludlow et al. (2013) we use the cosmological simulations from

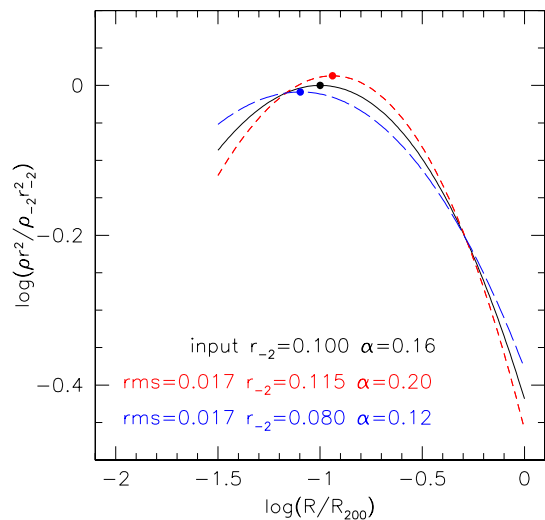


Figure 4. Illustration of the degeneracy between scale radius, r_{-2} , and shape parameter, α , for the Einasto profile. The black line shows a profile with $r_{-2} = 0.1$ and $\alpha = 0.16$ and the black circle shows the location of the scale radius. The red and blue lines show profiles with the same $rms = 0.017$. The red line has 25% higher α and 11% higher r_{-2} while the blue line has 25% lower α and 20% lower r_{-2} .

Dutton & Macciò (2014). These cover a similar halo mass range with similar resolution as those used by Ludlow et al. (2013). As with Ludlow et al. (2013) we only consider haloes containing at least $N = 5000$ particles. Fig. 3 shows the c vs halo mass (upper) and α vs halo mass (lower) relations at redshift $z = 0$, colour coded by α and c , respectively. These show very similar trends as reported by Ludlow et al. (2013), namely, at a given halo mass, higher c haloes have on average lower α .

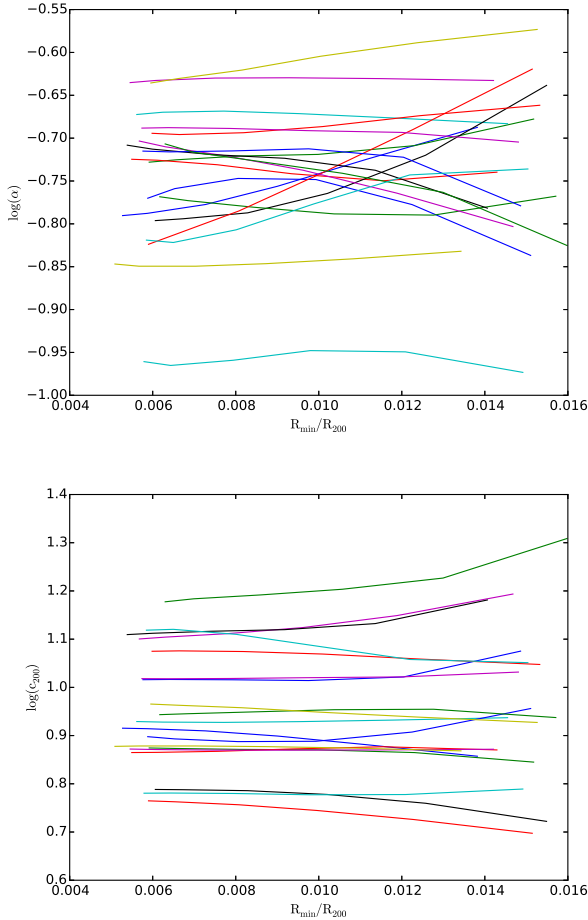


Figure 5. Impact of minimum radius on the fitted α (upper panel) and c (lower panel) for the Buck haloes. Each colour represents a different halo.

3.1 Impact of resolution on covariance between c and α

An important difference between the haloes used in Figs. 2 & 3 is the number of particles. The number of particles is directly related to the smallest scales that the simulation can resolve (Power et al. 2003). Fig. 3 and Ludlow et al. (2013) include haloes with as few as 5000 particles. Since these are cosmological volumes, the samples are dominated by haloes within an order of magnitude of the limit. The mean number of particles per halo for the simulations used in Fig. 3 is $N \sim 10000$. Recall that in Fig. 2 we only include haloes with at least 10^5 particles.

Since Ludlow et al. (2013) use cosmological boxes, lower mass haloes are poorer resolved. In their Fig. 2 one can clearly see that the scatter in both c and α is higher for poorer resolved haloes. By comparing results at a halo mass of $10^{13.6} M_{\odot}$ we see that the haloes from the largest box (and hence lowest resolution) have higher average α and lower average c than the haloes from the smallest (and hence higher resolution box). This shows an anti-correlation between α and c , plausibly due to fitting degeneracies.

By comparing Einasto density profiles with different α

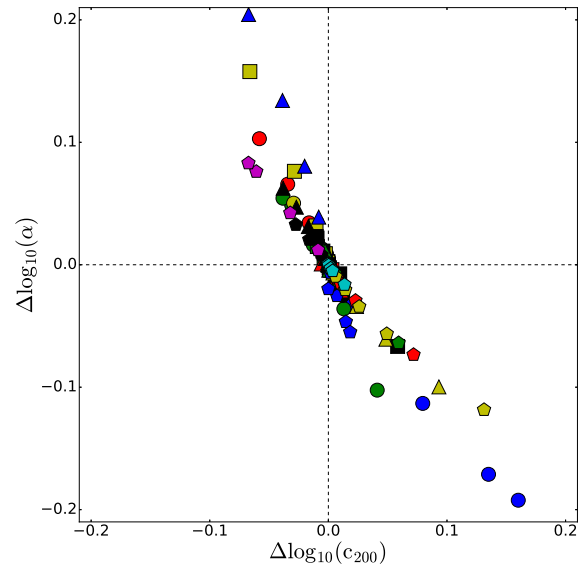


Figure 6. Covariance between fitted α and c . For each halo (different colour/symbol) we vary the minimum radius of the data used in the fit and plot the change in $\log \alpha$ and $\log c$ with respect to the highest resolution fit.

and scale radii, it is easy to see how a fitting degeneracy could occur. An example is shown in Fig. 4. For this example we chose typical values of the scale radius and α . All three profiles are normalized to the scale radius of the input halo. When α is increased (red line) the profile becomes more peaked, while lower α (blue line) results in a flatter profile. The deviations get larger the further away from the scale radius we go, so with a halo resolved to 1% of the virial radius there is a clear distinction between different α . For a less well resolved halo, e.g., minimum radius of 3% of the virial radius one can improve the fit by changing the scale radius (and overall normalization).

To investigate the role of resolution further we re-fit the Buck et al. haloes and vary the minimum radius of the density profile to mimic the effects of lower resolution simulations. In Fig. 5 we plot the resulting α and c vs the minimum radius used in the fit. We see that the fitted values are quite stable from one resolution to the next, but there are systematic shifts, so that the scatter in c and α increases with poorer resolution. In Fig. 6 we plot the change in α (with respect to the highest resolution fit) vs the change in c . Each colour/symbol corresponds to a different halo. There is a clear anti-correlation between α and c which confirms our suspicion that a fitting degeneracy is responsible for the anti-correlation between α and c found with lower resolution haloes.

Going a step further we create 1000 mock density profiles varying the halo mass from 10^9 to 10^{13} . We use the Einasto function and draw the parameters (α, c) from our fits at redshift $z = 0$. Each profile is sampled from 0.002 to $1.0 R_{200}$ with 15 equally log-spaced bins, with noise added to the density profile. We do a series of fits, successively removing the innermost bin. In Fig. 7 we plot the error on

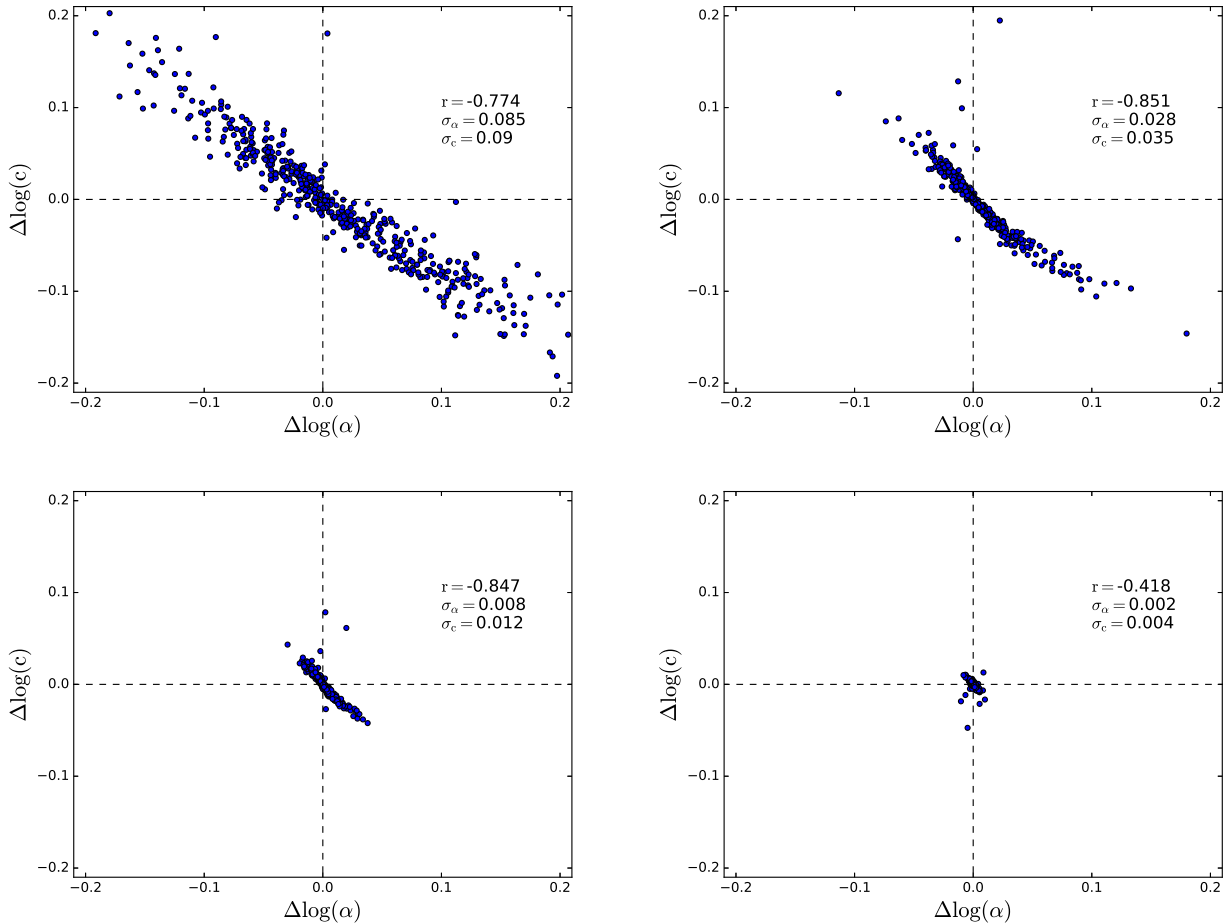


Figure 7. Covariance between errors on fitted α and c from fits to mock Einasto density profiles. Each panel corresponds to a different minimum radius and corresponding number of particles inside the virial radius: $N \approx 4000$ (top left); $N \approx 50000$ (top right); $N \approx 300000$ (bottom left); $N \approx 2$ million (bottom right). The numbers in the top right quadrant give the correlation coefficient, r , the standard deviation of $\Delta \log c$ and $\Delta \log \alpha$.

$\log(c)$ vs the error on $\log(\alpha)$ for all 1000 mocks. Each panel corresponds to a different R_{\min} . We relate the innermost bin to the number of particles in the virial radius using the convergence criteria of Power et al. (2003):

$$0.6 = \frac{N(R_{\text{conv}})}{8 \ln N(R_{\text{conv}})} \left(\frac{R_{\text{conv}} M(R_{\text{conv}})}{R_{200} M_{200}} \right)^{1/2}, \quad (3)$$

Given an $R_{\min} \equiv R_{\text{conv}}$, and a mass profile $M(R) \equiv m_p N(R)$, we solve for the number of particles within the virial radius.

For $N = 2$ million (lower left) the error on c and α is small $< 1\%$. With poorer resolved haloes the errors on the fitted c and α increase, to $\sim 7\%$ for $N = 50000$ (top right) and $\sim 23\%$ for $N = 4000$ (top left). But more importantly there is a clear anti-correlation between c and α for $N < 300000$. For the results in Fig.2 we use at least 10^5 particles and typically have 10^6 particles, and thus do not expect significant fitting degeneracies between c and α .

In summary we have shown using mock density profiles and re-samples of our simulated density profiles that poorer resolved haloes suffer a degeneracy between the fitted c and α . This reconciles our result of no correlation between

c and α (at fixed halo mass) obtained with a million particles per halo, with the strong correlation (at fixed halo mass) found by Ludlow et al. (2013) obtained with $\sim 10^4$ particles per halo. Since there is a strong correlation between c and mass accretion history, one might be tempted to conclude that our results imply no correlation between α and mass accretion history, and thus contradict the result found by Ludlow et al. (2013). However, the correlation reported by Ludlow et al. (2013) is a weak one, and there is scatter in the relation between c and mass accretion history. If this scatter depends on α , then it could reconcile our apparently contradictory results.

4 EVOLUTION OF MOST MASSIVE PROGENITORS

We have shown that there is no significant correlation between α and c at a given redshift for a sample of well resolved haloes. We now study the evolution of the most massive (and hence well resolved haloes) in the Buck et al. sample. At each redshift we have a sample of about 20 haloes. In order to probe halo masses below $\sim 10^{10} M_{\odot}$ and redshift

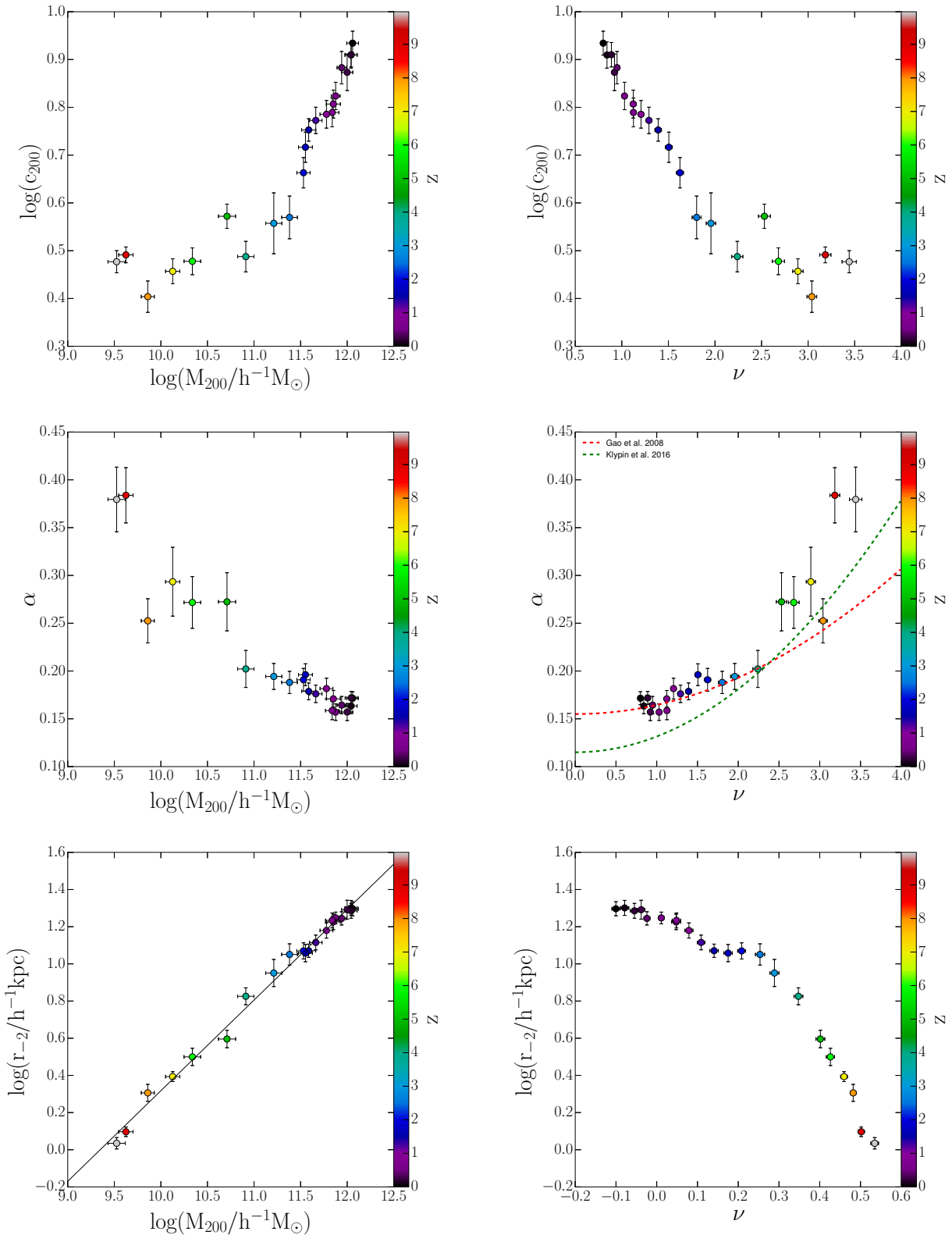


Figure 8. Evolution of the concentration, c , Einasto shape parameter, α , and scale radius, r_{-2} , vs halo mass, M_{200} (left), and peak parameter, ν (right). At each redshift, z (indicated by the colour), the median value for the most massive haloes in the Buck et al. simulations are plotted. The error bar corresponds to the error on the median. For the lower left plot, a power-law was fitted to the points (see Equation 3).

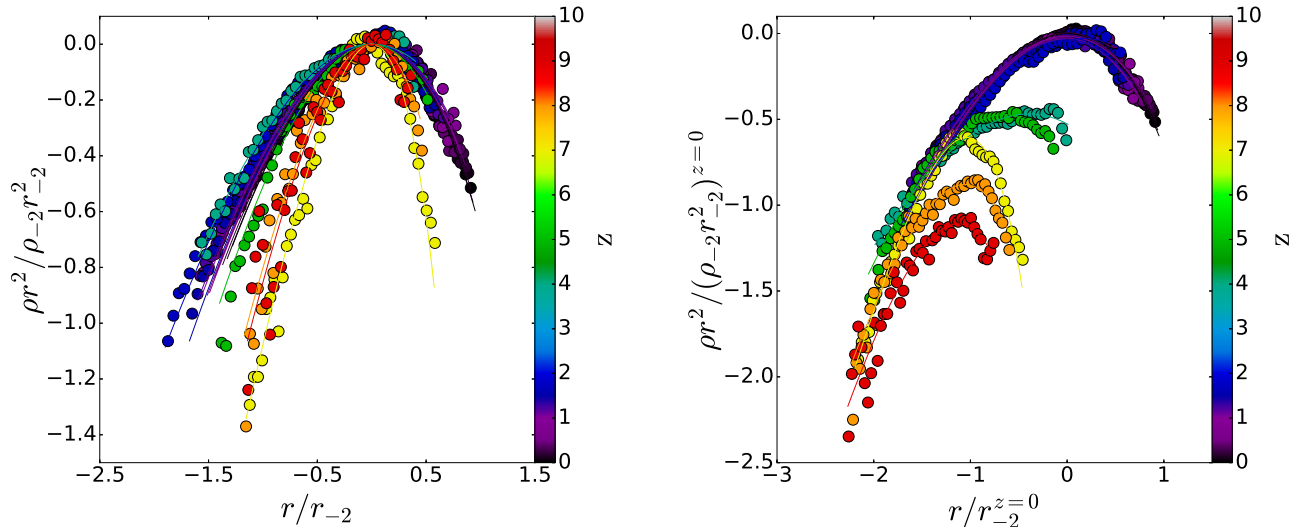


Figure 9. Evolution of the density profile (coloured points) and Einasto fits (solid lines) at different redshifts, for a $10^{12} M_{\odot}$ halo. For the left panel, the data and fits were normalized to the values of r_{-2} and $\rho_{-2} r_{-2}^2$ at each individual redshift, while for the right panel, the normalization is relative to the values of r_{-2} and $\rho_{-2} r_{-2}^2$ at redshift $z = 0$.

$z > 7$ we relax the criteria to include halos with at least 10^4 particles. The fits at the highest redshifts will thus be individually less reliable as those at lower redshifts, nevertheless, the poorer resolved haloes continue the trends set by the better resolved haloes. At each redshift we calculate the median concentration, shape parameter, and halo mass. The left-hand panels in Fig. 8 show the evolution of the c vs mass, α vs mass, and r_{-2} vs mass relations.

At early times ($z \sim 10$) haloes have low concentration, $c \simeq 3$, small scale radii, $r_{-2} \sim 1 h^{-1} \text{kpc}$ and high shape parameter $\alpha \simeq 0.4$. As the halo grows in mass the scale radius and concentration increases while the shape parameter decreases relatively smoothly. Thus for the most massive progenitor of a given halo, the evolution of c and α are anti-correlated. Interestingly there is a power-law relation between the scale radius and halo mass with a slope of roughly 1/2:

$$\log_{10} \left(\frac{r_{-2}}{[h^{-1} \text{kpc}]} \right) = 0.488 \log_{10} \left(\frac{M_{200}}{[10^{12} h^{-1} M_{\odot}]} \right) + 1.30. \quad (4)$$

In the right-hand panels we replace halo mass with the dimensionless peak height parameter, ν (see Eq. 2). The peak height of the most massive halo increases as we go back in time, so the plots with ν are almost a mirror reflection of the plots with mass. The middle panel shows the well known correlation between α and ν . The dashed and dotted lines show fitting formula from Gao et al. (2008) and Klypin et al. (2016), respectively which our simulations are broadly consistent with.

How does the density profile of the haloes evolve? The scale radius corresponds to the peak of the $r^2 \rho$ vs radius plot, while the shape parameter is sensitive to the density profile both at larger and smaller radii than r_{-2} . In Fig. 9 we show the evolution of the density profile of a single halo. The left panel shows profiles that have been normalized to the scale radius and scale density at each redshift. We clearly see higher redshift haloes have density profiles more concen-

trated (higher α) around the scale radius. Relative to the scale radius, mass is being added at both small and large radii with time. In the right panel the profiles are normalized to the scale radius and density at redshift $z = 0$. This shows that after the initial growth at $z > 7$ the evolution is primarily due to mass being added at physically large radii. By $z \sim 3$ the density profile is largely in place, and while the virial radius grows by pseudo evolution of the background density, the α and r_{-2} appear to continuously evolve.

5 DISCUSSION

As discussed in the introduction it has been suggested that the slope of the power-spectrum of density fluctuations determines the Einasto α parameter (Cen 2014; Nipoti 2015; Ludlow & Angulo 2017). If this were the sole explanation, then we would expect higher mass and ν haloes to have lower α in Λ CDM simulations. The fact the opposite is seen means there must be another explanation.

In our simulations we find the most massive progenitors of Milky Way mass haloes have high α , which subsequently decreases with increasing time. This is reminiscent of the violent relaxation process (Lynden-Bell 1967) of dissipationless major mergers which tends to decrease α towards, but does not reach, the isothermal value ($\alpha = 0$). We thus speculate that it is the evolutionary state of the halo that determines α .

The connection with the power-spectrum slope is due to the fact that in a given amount of time, major mergers have a much larger relaxation effect than an equivalent sum of minor mergers (Hilz et al. 2012). This is related to the fact the dynamical friction time scale, $t_{\text{df}} \propto (M/m)/\ln(M/m)$, where M/m is the mass ratio, is shorter for major mergers. Thus the haloes formed from flat spectra will experience more major mergers and are expected to be more dynami-

cally evolved than haloes of the same mass that form from steep spectra via minor mergers.

We expect the evolutionary trend of α decreasing is also true for higher and lower mass haloes (because of the α vs ν relation appears independent of redshift). Nevertheless, it would be worth verifying this with high-resolution simulations.

6 SUMMARY

We use high resolution (up to 10 million particles per halo) N-body zoom-in simulations to study the structure of dwarf to Milky Way mass dark matter haloes over cosmic time. We fit our haloes with the three parameter Einasto function, specified by the halo mass, concentration, c , and profile shape, α . We summarize our results as follows:

- At a given redshift, α is independent of c (Fig. 2). This means that (at least) three parameters are needed to accurately describe the structure of Λ CDM haloes.
- We trace previous reports (Ludlow et al. 2013) of a strong anti-correlation between α and c to a fitting degeneracy in lower resolution ($\sim 10^4$ particles per halo) simulations (Figs. 6 & 7).
- However, for the most massive progenitors of individual haloes the evolution in α and c is anti-correlated (Fig. 8). At high redshift ($z \sim 7$) $\alpha \sim 0.3$ and $c \sim 3$. As the halo evolves α decreases while c increases.
- The increase in concentration is due to an increase in virial radius, which more than compensates for the increase in scale radius, r_{-2} with time (Fig. 8).
- The evolution of halo structure (α and r_{-2}) is primarily due to accretion of mass at large radii (Fig. 9).

We speculate that the evolution of α is related to the relaxation state of the halo. Younger, less dynamically relaxed haloes have higher α closer to a spherical top hat, while older, more dynamically relaxed haloes have lower α closer to an isothermal. Studying the dynamics of the halo particles would be a way to verify this.

ACKNOWLEDGMENTS

We thank the anonymous referee whose comments helped to improve the clarity of the paper. This research was carried out on the High Performance Computing resources at New York University Abu Dhabi; on the THEO cluster of the Max-Planck-Institut für Astronomie and on the HYDRA clusters at the Rechenzentrum in Garching. We greatly appreciate the contributions of all these computing allocations.

REFERENCES

- Buck, T., Macciò, A. V., & Dutton, A. A. 2015, *ApJ*, 809, 49
 Buck, T., Dutton, A. A., & Macciò, A. V. 2016, *MNRAS*, 460, 4348
 Bullock, J. S., Kolatt, T. S., Sigad, Y., et al. 2001, *MNRAS*, 321, 559
 Cen, R. 2014, *ApJ*, 790, L24
 de Blok, W. J. G., Walter, F., Brinks, E., et al. 2008, *AJ*, 136, 2648-2719

- Dubinski, J., & Carlberg, R. G. 1991, *ApJ*, 378, 496
 Dutton, A. A., van den Bosch, F. C., Dekel, A., & Courteau, S. 2007, *ApJ*, 654, 27
 Dutton, A. A., & van den Bosch, F. C. 2009, *MNRAS*, 396, 141
 Dutton, A. A., & Macciò, A. V. 2014, *MNRAS*, 441, 3359
 Einasto, J. 1965, *Trudy Astrofizicheskogo Instituta Alma-Ata*, 5, 87
 Foreman-Mackey, D., Hogg, D. W., Lang, D., & Goodman, J. 2013, *PASP*, 125, 306
 Gao, L., Navarro, J. F., Cole, S., et al. 2008, *MNRAS*, 387, 536
 Gill, S. P. D., Knebe, A., & Gibson, B. K. 2004, *MNRAS*, 351, 399
 Hernquist, L. 1990, *ApJ*, 356, 359
 Hilz, M., Naab, T., Ostriker, J. P., et al. 2012, *MNRAS*, 425, 3119
 Klypin, A., Yepes, G., Gottlöber, S., Prada, F., & Heß, S. 2016, *MNRAS*, 457, 4340
 Knollmann, S. R., & Knebe, A. 2009, *ApJS*, 182, 608
 Lynden-Bell, D. 1967, *MNRAS*, 136, 101
 Ludlow, A. D., Navarro, J. F., Boylan-Kolchin, M., et al. 2013, *MNRAS*, 432, 1103
 Ludlow, A. D., & Angulo, R. E. 2017, *MNRAS*, 465, L84
 Macciò, A. V., Dutton, A. A., van den Bosch, F. C., et al. 2007, *MNRAS*, 378, 55
 Moore, B. 1994, *Nature*, 370, 629
 Muñoz-Cuartas, J. C., Macciò, A. V., Gottlöber, S., & Dutton, A. A. 2011, *MNRAS*, 411, 584
 Navarro, J. F., Frenk, C. S., & White, S. D. M. 1996, *ApJ*, 462, 563
 Navarro, J. F., Frenk, C. S., & White, S. D. M. 1997, *ApJ*, 490, 493
 Navarro, J. F., Ludlow, A., Springel, V., et al. 2010, *MNRAS*, 402, 21
 Nipoti, C. 2015, *ApJ*, 805, L16
 Power, C., Navarro, J. F., Jenkins, A., et al. 2003, *MNRAS*, 338, 14
 Prada, F., Klypin, A. A., Cuesta, A. J., Betancort-Rijo, J. E., & Primack, J. 2012, *MNRAS*, 423, 3018
 Wang, L., Dutton, A. A., Stinson, G. S., et al. 2015, *MNRAS*, 454, 83